Earth and Planetary Science Letters 492 (2018) 144–151

Contents lists available at ScienceDirect

Earth and Planetary Science Letters

www.elsevier.com/locate/epsl

A basal magma ocean dynamo to explain the early lunar magnetic field

Aaron L. Scheinberg [a,*], Krista M. Soderlund [b], Linda T. Elkins-Tanton [c]

[a] Princeton Plasma Physics Laboratory, Princeton, NJ 08543, USA
[b] Institute for Geophysics, Jackson School of Geosciences, University of Texas at Austin, Austin, TX 78758, USA
[c] School of Earth and Space Exploration, Arizona State University, Tempe, AZ 85287, USA

ARTICLE INFO

Article history:
Received 18 September 2017
Received in revised form 5 February 2018
Accepted 9 April 2018
Available online 16 April 2018
Editor: B. Buffett

Keywords:
lunar magnetism
geodynamo
magma ocean
geodynamics

ABSTRACT

The source of the ancient lunar magnetic field is an unsolved problem in the Moon's evolution. Theoretical work invoking a core dynamo has been unable to explain the magnitude of the observed field, falling instead one to two orders of magnitude below it. Since surface magnetic field strength is highly sensitive to the depth and size of the dynamo region, we instead hypothesize that the early lunar dynamo was driven by convection in a basal magma ocean formed from the final stages of an early lunar magma ocean; this material is expected to be dense, radioactive, and metalliferous. Here we use numerical convection models to predict the longevity and heat flow of such a basal magma ocean and use scaling laws to estimate the resulting magnetic field strength. We show that, if sufficiently electrically conducting, a magma ocean could have produced an early dynamo with surface fields consistent with the paleomagnetic observations.

1. Introduction

Apollo samples of lunar crust indicate a surface field of ∼77 μT that was present between 4.2 and 3.56 Ga and likely continued at a lower magnitude for billions of years (Tikoo et al., 2017; Garrick-Bethell et al., 2017; Weiss and Tikoo, 2014; Suavet et al., 2013; Shea et al., 2012). Considering the large uncertainty in the paleomagnetic field inferred from measurement of these samples, a model that predicts at least ∼35 μT during the early high-field epoch would be consistent with observation (Weiss and Tikoo, 2014). However, numerical modeling of an Earth-like dynamo driven by thermochemical core convection instead predicts magnitudes of $\lesssim$1 μT (Stegman et al., 2003; Evans et al., 2014, 2018; Laneuville et al., 2014; Scheinberg et al., 2015). Dwyer et al. (2011) considered tidal forcing as an additional energy source for the dynamo, while Le Bars et al. (2011) considered impact-driven differential rotation. These alternative mechanisms are more promising, but the estimated magnetic fields are still several times lower than measurements ($\lesssim$9 μT and 4 μT, respectively).

Obtaining the observed lunar field magnitude with a core dynamo is particularly challenging because of the proportionally small lunar core. Dipole fields decay as $1/r^3$, where r is the distance from the dipole center. On Earth, this means that the dipole field at the surface is smaller than the dipole field at the core–mantle boundary by a factor of $\sim(6370\text{ km})^3/(3400\text{ km})^3 = 6.6$. In contrast, given the lunar radius of 1737 km and a core radius in the range 200–380 km (Williams et al., 2014), the dipole field of a core dynamo is 100–700 times smaller at the surface than at the core–mantle boundary. However, if the dynamo originated in a region extending to within 800 km of the surface, the field would be reduced only by a factor of ten from the dynamo to the surface.

1.1. Basal magma ocean formation

The Moon is believed to have become largely molten during its formation due to heat of accretion, radiogenic heating, and tidal forces (Warren, 1985). This magma ocean may have comprised as much as the upper 1000 km of the Moon, and have remained molten for as long as 200 m.y. due to continued tidal interactions with Earth (Meyer et al., 2010). Fractional crystallization is also highly likely to have occurred. In this scenario, crystals forming in the magma ocean would have settled to the bottom and sequestered themselves from chemical equilibrium with the remaining liquid, causing an evolving liquid composition in the magma ocean. The final, highly evolved liquids, the 'ur-KREEP', would have contained the majority of all incompatible elements, not just the potassium, rare Earth elements, and phosphorus for which they are named. These last liquids would also contain the majority of the uranium and thorium, which, together

* Corresponding author.
E-mail address: scheinberg@princeton.edu (A. Scheinberg).

https://doi.org/10.1016/j.epsl.2018.04.015
0012-821X/

with potassium, are responsible for most of the radiogenic heating on Earth.

Fractional solidification of the global lunar magma ocean would have resulted in a gravitationally unstable mantle profile (Spera, 1992). Solidification models show that the density contrast between the KREEP layer and the remaining mantle range from $\Delta\rho = 300$–$500\ \mathrm{kg\,m^{-3}}$, depending on the amount of interstitial fluid trapped within the solidified cumulate (Elkins-Tanton et al., 2011). These models further suggest a large amount of KREEP material, $2{\cdot}10^9\ \mathrm{km^3}$ or ∼9% of the mantle by volume. Though initially located just underneath the plagioclase crust, at least some fraction of this material would have overturned due to gravitational instability and formed a dense, radiogenic mantle layer located just above the core. This fraction is poorly constrained; in Appendix A, we provide a basic model indicating anywhere from 0 to 1 is plausible. If settled in its entirety on the core–mantle boundary (CMB), the material would constitute a ∼450 km-thick layer.

Previous studies adopted significantly smaller values of $\Delta\rho$ (45–90 $\mathrm{kg\,m^{-3}}$) (Stegman et al., 2003; Zhang et al., 2013; Scheinberg et al., 2015). In those studies, thermal expansion of the KREEP layer was sufficient to overcome the compositional density difference, causing the material to re-mix into the overlying mantle. In contrast, using $\Delta\rho = 300$–$500\ \mathrm{kg\,m^{-3}}$, the KREEP layer would remain sequestered at the CMB. Highly radiogenic and still near its solidus temperature, the layer would fully melt. The result would be a metalliferous basal magma ocean (BMO) that persists until convective heat loss across the overlying solid mantle causes ocean solidification. Indeed, recent modeling by Zhang et al. (2017) concluded that a relatively stable, partially molten, ilmenite-bearing cumulates layer may surround the lunar core to present day.

1.2. A basal magma ocean dynamo

Ziegler and Stegman (2013) showed that a basal magma ocean on Earth could potentially drive a dynamo if it is unstable to convection and has sufficient electrical conductivity, σ. This requirement is manifested in a magnetic Reynolds number, which must exceed a critical value for magnetic field generation to occur (Roberts, 2007): $Rm_c \gtrsim 10$. This parameter relates the Ohmic diffusion timescale to the convective timescale and is defined as $Rm = \mu_0 \sigma U L$, where U and L are the system's characteristic velocity and length scale, respectively, and μ_0 is the permeability of free space.

The principle difficulty of a magma ocean dynamo hypothesis is that silicate material has a far lower electrical conductivity than a metallic iron-alloy core. However, the BMO is expected to have a relatively large electrical conductivity due to its molten nature and its particularly high titanium and iron contents (van Kan Parker et al., 2012; Khan et al., 2014; Elkins-Tanton et al., 2011). Using olivine melts at lunar mantle conditions as a lower bound (Pommier et al., 2015), we anticipate $\sigma > 80$ S/m. The presence of Fe–Ti oxides in terrestrial rocks is observed to increase the electrical conductivity up to three orders of magnitude (Bartetzko et al., 2005), suggesting an upper bound of $\sigma \sim 10^4$ S/m. More recently, experimental work by Lin et al. (2017a) and Lin et al. (2017b) argues for a substantial water component in the Moon and suggests that the deep magma ocean was extremely iron rich. Sufficient conductivity is thus plausible, though it cannot be definitively inferred from available evidence. Fortunately, the basic BMO dynamo hypothesis can be studied regardless of the uncertainty in lunar interior composition.

In this study, we estimate the longevity and heat flow of such a basal magma ocean, calculate the critical conductivity σ_{crit} above which dynamo action can be maintained, and predict the resulting magnetic field strength.

2. Methods

To simplify the analysis, we assume that three events have already occurred: (1) the magma ocean has solidified; (2) mantle overturn has caused some percentage of the dense layer to fall to the CMB while a fraction f_{KREEP} remained stuck directly beneath the plagioclase lid; and (3) sufficient heating to completely remelt this fallen material has occurred. We initiate the models at 4.2 Ga, when paleomagnetic observations indicate the field began and after which overturn and melting has occurred. (The time of initialization affects only the model's radiogenic heating values. If the model began at 4.3 Ga instead, initial radiogenic heating levels would be 5% higher.) As initial conditions, we assume a fully molten basal magma ocean at 1700 K, a homogeneous temperature of 1500 K within the solid cumulate mantle, and a conductive thermal profile in the upper 250 km. The thickness of this conductive layer is somewhat arbitrary, but is only an initial condition; once a simulation is launched, mantle convection will result in a thermal profile consistent with the input parameters of that simulation.

Radiogenic heating within the BMO will initially cause a temperature increase. When it cools back to the initial temperature, the model run is stopped. Furthermore, the fully molten core is presumed to contain enough sulfur ($\gtrsim$4%) that its liquidus temperature, which is strongly dependent on sulfur content, is never reached during a model run. These two model restrictions enable us to avoid the additional complexity (and associated assumptions) of solidification of the basal magma ocean and core while still determining the ocean's lifetime and potential dynamo action. Melting of the overlying solid cumulate materials and their assimilation into the BMO is similarly neglected since such melt would be buoyant compared to the surrounding solid mantle.

2.1. Solid mantle model

We use the spherical finite-element model CitcomS to simulate convection in the solid portion of the mantle. The model assumes that the mantle, excluding the basal magma ocean (BMO), is an incompressible spherical shell and that variations in density affect the equations of motion only through changes in buoyancy (the Boussinesq approximation). Mantle evolution is computed by iteratively solving the conservation equations for mass, momentum, and energy (see Zhong et al., 2008, for details). The numerical grid consists of 12 regions with $36 \times 36 \times 48$ elements each, providing a vertical and average horizontal resolution of approximately 30 km. Our lowest-viscosity (and therefore least resolved) simulation was repeated with 2.4× the volumetric resolution ($49 \times 49 \times 65$). The resulting fields were within 2%, indicating sufficient resolution.

The lunar surface temperature is held constant at 250 K. The upper 60 km is buoyant and thus behaves as a cold, stagnant lid crust. The temperature at the magma ocean boundary, T_{B}, is coupled to the BMO model described in the next section. The material parameters employed in the model are listed in Table 1. Our chosen geometry and parameter values are consistent to within 1% with present-day mass and moment of inertia measurements (Williams et al., 2014).

Solid mantle viscosity is temperature-dependent and determined by a Newtonian Arrhenius equation:

$$\mu = \mu_0^* \exp\left[\frac{E}{R_g T} - \frac{E}{R_g T_{ref}}\right], \tag{1}$$

where $E = 150$ kJ/mol is the effective activation energy, R_g is the ideal gas constant, and reference temperature T_{ref} is 1300 °C (Christensen, 1984; Karato and Wu, 1993). We vary the reference viscosity over $\mu_0^* = 10^{18}$–10^{20} Pa s.

Table 1
Fixed model parameters.

Symbol	Description	Value
R	Lunar radius	1737 km
R_C	Core radius[a]	350 km
ρ_m	Reference mantle density[b]	3400 kg m^{-3}
ρ_c	Core density[c]	7800 kg m^{-3}
g_o	Surface gravity[b]	1.6 m s^{-2}
Ω	Rotational velocity	$2\pi/27.3$ rad d^{-1}
$c_{P,m}$	Specific heat, mantle[c]	1250 J kg^{-1} K^{-1}
$c_{P,b}$	Specific heat, basal magma ocean	1250 J kg^{-1} K^{-1}
$c_{P,c}$	Specific heat, core[d]	835 J kg^{-1} K^{-1}
κ_m	Thermal diffusivity, mantle[c]	$1{\cdot}10^{-6}$ m^2 s^{-1}
k_b	Thermal conductivity, basal magma ocean	4 W m^{-1} K^{-1}
k_c	Thermal conductivity, core[e]	40 W m^{-1} K^{-1}
α_m	Thermal expansivity, mantle[c]	$3{\cdot}10^{-5}$ K^{-1}
α_b	Thermal expansivity, basal magma ocean[f]	$5{\cdot}10^{-5}$ K^{-1}
α_c	Thermal expansivity, core[g]	$9.2{\cdot}10^{-5}$ K^{-1}
T_{surf}	Surface temperature	250 K
E	Activation energy[h]	150 kJ mol^{-1}
c_U	Uranium concentration[i]	0.039 ppm
c_K	Potassium concentration[i]	212 ppm
c_{Th}	Thorium concentration[i]	0.15 ppm
c	Proportionality constant[j]	0.63

[a] Williams et al. (2014).
[b] Stegman et al. (2003).
[c] Zhang et al. (2013).
[d] Desai (1986).
[e] Touloukian et al. (1970).
[f] Solomatov (2007).
[g] Anderson and Ahrens (1994).
[h] Scheinberg et al. (2015).
[i] Hagerty et al. (2006).
[j] Christensen (2010).

The total radiogenic heating in the Moon is given by:

$$H = M\sum_i c_i x_i h_i e^{\lambda_i t} \tag{2}$$

where M is the mass of the mantle and crust, the index i refers to U_{235}, U_{238}, K_{40}, or Th_{232}, c_i is the element's estimated present-day average concentration in ppm, x_i is the present-day isotopic fraction, h_i is the power produced per unit mass of the isotope, λ_i is its decay constant, and t is time before present day.

The distribution of radiogenic heating is controlled by two parameters. f_{rad} is the fraction of radioactive material concentrated in the KREEP layer. $f_{\text{rad}} = 1$ would therefore indicate that all internal heating occurs in this material, while $f_{\text{rad}} \approx 0.09$ would indicate that heating is evenly distributed throughout the mantle and crust. f_{KREEP} is the fraction of the KREEP layer that remains trapped near the surface. (Note consequently that f_{KREEP} also determines the thickness of the BMO.) The total radiogenic heating within the solid mantle is therefore described as:

$$H_m = H(1 - f_{\text{rad}} + f_{\text{KREEP}} f_{\text{rad}}), \tag{3}$$

while the total radiogenic heating within the basal magma ocean is

$$H_b = H - H_m = H(1 - f_{\text{KREEP}}) f_{\text{rad}}. \tag{4}$$

2.2. Basal magma ocean and core model

Both the BMO and the core are well-mixed on the timescales of the overlying solid mantle convection and can thus be treated with a one-dimensional model. The BMO and core are assumed to have an adiabatic temperature gradient. (In the core, this will not be true during the phase in which the magma ocean increases in temperature; however due to the core's small size and its high thermal conductivity, the impact of this assumption on mantle evolution is negligible.) The temperature within the BMO is given by

$$T(r) = T_{\text{B}} \exp\left[\frac{R_{\text{B}}^2 - r^2}{D_b^2}\right], \tag{5}$$

where R_{B} is the BMO's outer radius (top of the dynamo region) and T_{B} is the temperature at R_{B} (Labrosse, 2003). D_b is a length scale defined by $D_b = \sqrt{3c_{P,b}/(2\pi\alpha_b\rho_b G)} \sim 5{,}400$ km, where $c_{P,b}$ is the BMO's specific heat capacity, α_b is its thermal expansivity, ρ_b its density and G is the gravitational constant. Within the core, the temperature is given by

$$T(r) = T_{\text{C}} \exp\left[\frac{R_{\text{C}}^2 - r^2}{D_c^2}\right] = T_{\text{B}} \exp\left[\frac{R_{\text{B}}^2 - R_{\text{C}}^2}{D_b^2} + \frac{R_{\text{C}}^2 - r^2}{D_c^2}\right] \tag{6}$$

where T_{C} and R_{C} are the temperature and radius of the core–mantle boundary, respectively, and $D_c \sim 3{,}000$ km is the analogous length scale to D_b for core material parameters. The second equality of Eq. (6) is obtained by determining T_{C} from Eq. (5). This is possible since the boundary layer thickness between the two liquids, and consequently the temperature difference across it, is negligibly small. Having assumed spherical symmetry, secular cooling of these two regions is equal to radiogenic internal heating, H_b, minus the heat flow outward across the BMO boundary, Q_{B}:

$$\int_0^{R_{\text{B}}} \rho(r) c_P(r) \frac{\partial T(r)}{\partial t} 4\pi r^2 dr = H_b - Q_{\text{B}}. \tag{7}$$

The temperature at the magma ocean boundary, T_{B}, is spatially uniform since the BMO below is presumed to be well-mixed. Combining equations (5)–(7) and evaluating the integral, we find that

$$\frac{\partial T_{\text{B}}}{\partial t}(c_{P,c}\rho_c V_c I_c + c_{P,b}\rho_b V_b I_b) = H_b - Q_{\text{B}}, \tag{8}$$

where I_c and I_b are constants dependent on the geometry and physical properties of the system. In our models, these constants are greater than one but do not exceed 1.018 and 1.008, respectively. Setting $I_c = I_b = 1$ yields:

$$\frac{\partial T_{\text{B}}}{\partial t} = \frac{H_b - Q_{\text{B}}}{c_{P,c}\rho_c V_c + c_{P,b}\rho_b V_b}. \tag{9}$$

Here, ρ_c, ρ_b, $c_{P,c}$, $c_{P,b}$ are the density and specific heat capacity of the core and BMO, respectively. The same specific heat capacity is used for the BMO and the mantle. V_c and V_b are the volumes of the core and basal magma ocean, respectively. Q_{B} is computed at each time step from the horizontally averaged temperature difference between the lowest two node layers of the numerical model. We then use equation (9) to determine the change in temperature at each model time step, then use the new T_{B} as the lower boundary temperature of the solid-state convection model in the next time step.

2.3. Magnetic field scalings

The BMO will be unstable to thermal convection if heat flow is superadiabatic. Scaling laws relate the associated convective power, ϕ, to anticipated convective velocities and dynamo amplitudes. Different characteristic velocities can be estimated with scaling arguments that derive from assumptions about the dominant force balances in the BMO. With this information, we can estimate the magnetic field by equating magnetic energy to a fraction of available power (Christensen, 2010):

$$\frac{B^2}{2\mu_0} = c f_{ohm} \frac{L}{U} \phi, \tag{10}$$

where B is the magnetic field strength within the BMO, μ_0 is magnetic permeability, $c = 0.63$ is a constant of proportionality, U is the characteristic convective velocity, and $L = R_B$ is the characteristic length scale equal to the radius of the upper BMO boundary. f_{ohm} represents the ratio of Ohmic to total dissipation. If kinematic viscosity ν is much less than magnetic diffusivity λ then viscous heating can be neglected (Braginsky and Roberts, 1995); in this case f_{ohm} is ~1. Using recent experimental results suggesting magma ocean viscosity $\mu \sim 1$ Pa s (Dygert et al., 2017), we find that $\nu = \mu/\rho = 10^{-3}$ m^2/s. For $\sigma = 10^4$ S/m, λ is $\sim 10^2$ m^2/s, suggesting that $f_{ohm} \sim 1$ (typically assumed for planetary cores) is also applicable in a lunar basal magma ocean.

The volumetric power thermodynamically available to drive a dynamo, ϕ, can be formulated in several equivalent manners (Christensen, 2010; Lister and Buffett, 1995; Lister, 2003; Nimmo, 2007). We use a buoyancy-flux formulation (Buffett et al., 1996; Buffett, 2002) for its clarity:

$$\phi = \frac{1}{V_b} \frac{\alpha}{c_P} Q_B^* \left[\psi(R_B) - \bar{\psi} \right], \tag{11}$$

where ψ is gravitational potential and $\bar{\psi}$ is average gravitational potential in the BMO. Superadiabatic heat flow across the upper BMO boundary is given by $Q_B^* = Q_B - Q_{ad}$, where $Q_{ad} = 16\pi^2 G \rho_b \alpha_b k_b T_B R_B^3/(3 c_{P,b})$ and k_b is the BMO's thermal conductivity. Since thermal and electrical conductivity are related, k_b should vary as we vary σ. However, Q_{ad} is effectively negligible in our models as it is less than 1–6% of Q_B even assuming thermal conductivity of the BMO is equal to that of the core.

Mixing length theory assumes a balance between inertial and buoyancy forces. As shown in Christensen (2010), this assumption produces a characteristic velocity $U = (\phi R_B/\rho_b)^{(1/3)}$. Substituting the mixing length characteristic velocity into equation (10) and solving for B yields

$$B_{ML}^2 = 2\mu_0 c (\rho_b R_B^2 \phi^2)^{1/3}. \tag{12}$$

Assuming a balance of Coriolis, inertial, and gravitational (Archimides) forces (the CIA scaling) yields $U = (\phi/\rho_b)^{2/5} (R_B/\Omega)^{1/5}$, where Ω is the angular velocity of the Moon, and

$$B_{CIA}^2 = 2\mu_0 c (\rho_b^2 R_B^4 \Omega \phi^3)^{1/5}. \tag{13}$$

Finally, the MAC (Magneto-Archimedes–Coriolis) scaling assumes a balance between Lorentz, gravitational and Coriolis forces. This balance yields a characteristic velocity $U = (\phi/\rho_b \Omega)^{1/2}$ and magnetic field magnitude

$$B_{MAC}^2 = 2\mu_0 c (\rho_b R_B^2 \Omega \phi)^{1/2}. \tag{14}$$

Christensen (2010) evaluated the suitability of scaling laws by fitting them to known terrestrial dynamos, and found empirically that the ML scaling was the most consistent fit. However, alternative scalings should also be considered, particularly since a basal magma ocean dynamo might not scale the same way as an Earth-like core dynamo.

We use the present day value of angular velocity Ω in our calculations. This is a lower limit since angular velocity was perhaps twice its current value in early lunar history; however, it does not strongly influence the result, since B_{CIA} and B_{MAC} scale as $\Omega^{1/10}$ and $\Omega^{1/4}$, respectively.

Poloidal components of the magnetic field will reach the surface while toroidal components will not. The partitioning of energy into these components is not known, but a pre-factor of 1/7 is commonly used to estimate the dipole component in the literature (e.g., Christensen and Aubert, 2006; Scheinberg et al., 2015) and is applied here. Including upward continuation of the potential field to the surface at radius R, the surface fields are thus estimated as

$$B_{surf} = \frac{1}{7} B r_B^3, \tag{15}$$

where $r_B = R_B/R$ is the ratio of the top of the dynamo region to the planet radius. Since magnetic field strength is independent of electrical conductivity, we are able to estimate the dynamo amplitude without speculating on this value and to separately estimate the conductivity necessary to meet the magnetic Reynolds number criterion.

From equations (12)–(14), it is clear that the scaling estimates are not highly sensitive to the parameters within them: a 1000-fold increase in heat flux would only change the ML estimate by a factor of 10. However, as discussed in the Introduction, the surface field is highly sensitive to r_B. Thus, a magma ocean dynamo is more conducive to strong surface magnetic fields than a core dynamo.

Table 2
Model runs. The first row shows our nominal run, V19K50p54. The name indicates the parameters chosen: 'V19' indicates a reference viscosity of 10^{19} Pa s and 'K50' indicates that 50% of the KREEP layer remained trapped near the surface ($f_{KREEP} = 0.5$). 'p54' indicates that 54% of internal heating is concentrated in the KREEP layer ($f_{rad} = 0.54$), or, equivalently, that the KREEP layer has concentrations 6× higher than the bulk mantle since it comprises 9% of the mantle. The peak surface magnetic field strength, B_{max}, and critical electrical conductivity for dynamo action, σ_{crit}, correspond to the ML, CIA, and MAC scaling laws, respectively.

Model	Thickness (km)	Lifetime (10^9 yr)	B_{max} (μT)	σ_{crit} (10^3 S/m)
V19K50p54	301	2.6	4.1, 6.8, 14	2.6, 7.3, 34
V20K50p54	301	6.4	4.0, 6.6, 14	2.6, 7.4, 34
V18.5K50p54	301	1.2	4.2, 7.0, 15	2.6, 7.4, 35
V18K50p54	301	0	–	–
V19K50p36	301	2.0	3.7, 6.1, 13	3.0, 8.7, 42
V19K50p18	301	0	–	–
V19K50p100	301	3.8	5.1, 8.2, 17	2.1, 5.6, 25
V20K50p100	301	9.7	4.9, 8.0, 17	2.1, 5.6, 25
V19K25p54	383	2.9	6.5, 11, 24	1.9, 5.4, 26
V19K00p54	450	3.1	9.2, 15, 34	1.5, 4.4, 21
V18K00p100	450	2.1	12, 19, 40	1.3, 3.4, 15
V19K50p27	301	1.6	3.4, 5.8, 13	3.4, 9.8, 49

3. Results

We investigate different scenarios by scanning across three parameters (Table 2). First, we vary reference viscosity μ_0^* in the solid mantle. Second, we vary f_{KREEP}, the fraction of the KREEP layer that remains near the surface. Finally, we vary f_{rad}, the fraction of radioactive material concentrated in the layer.

Fig. 1A shows a temperature cross-section of our nominal model. In all cases, the magma ocean exhibits a rapid increase in temperature, followed by a steady decline until reaching the initial temperature (Fig. 1B). Even as the magma ocean is heated significantly beyond its melting temperature, temperatures in the solid mantle remained lower, with the exception of its lower boundary layer. Although not modeled explicitly, this small amount of bulk mantle melt could have resulted in a low effective mantle viscosity and also contributed to lunar magmatism.

BMO longevity results are presented in Table 2 and Fig. 2A. In our nominal model, we assume that 50% of the KREEP layer sank to the CMB, resulting in a BMO that is 301 km thick. Assuming 54% of radiogenic elements were concentrated in this material (thus 27% in the BMO, and 6× more concentrated than the bulk mantle) and a reference viscosity of 10^{19} Pa s, then the BMO would cool back

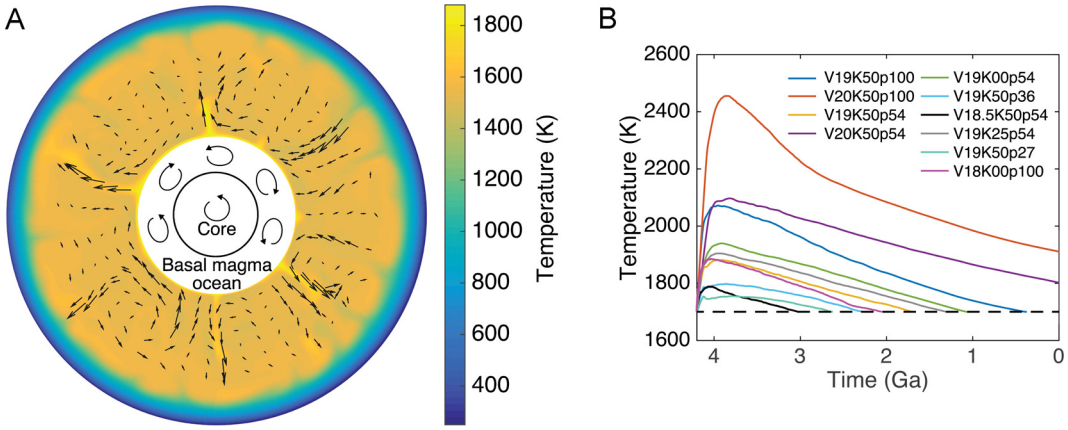

Fig. 1. Simulated temperature profile across the equatorial plane of the solid mantle and thermal evolution of the basal magma ocean boundary. **(A)** Convective patterns for the nominal model at 4 Ga suggest that plumes resulting from BMO heating may have been a cause of early recorded magmatism. However, in our models such upwellings are evenly distributed, so this mechanism alone does not account for the lack of mare basalts on the Moon's far side. **(B)** Simulated BMO boundary temperatures. Low-viscosity models cool off the fastest as heat is transferred efficiently from the BMO across the solid mantle. In contrast, the highest temperatures are reached when radiogenic heating is highly concentrated in the BMO and solid mantle viscosity is high.

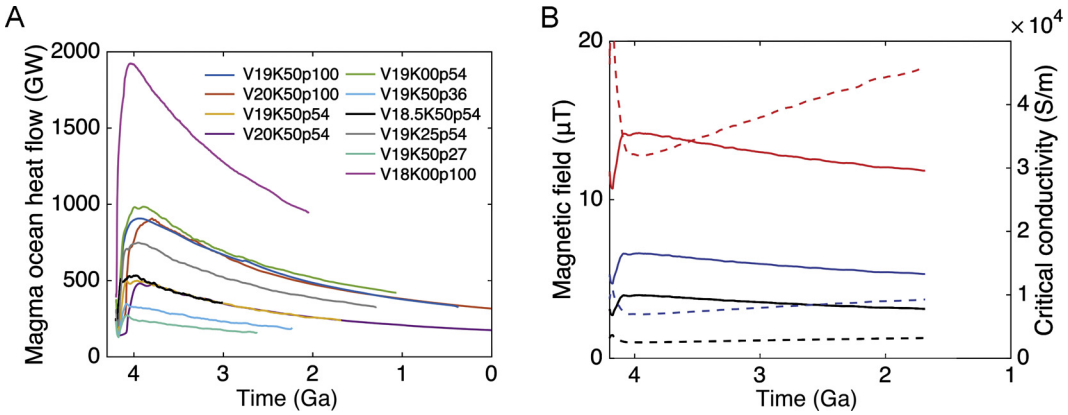

Fig. 2. Basal magma ocean heat flow and magnetic field generation. **(A)** Simulated heat flow across the BMO boundary. Heat flow (and consequently the power available to a dynamo) is highest if the BMO is large and highly radiogenic. **(B)** Predicted magnetic field strength (solid lines) and critical electrical conductivity to facilitate dynamo action (dashed lines) for the nominal model as a function of time. Colors indicate which velocity scaling law was used: ML (black), CIA (blue), and MAC (red).

to its initial temperature in 2.6 billion years (b.y.). Increasing viscosity by an order of magnitude reduces the efficiency of heat flow across the solid mantle and raises the lifetime to 6.4 b.y., implying a fully molten basal layer at present day. On the other hand, for a low reference viscosity of 10^{18} Pa s, convective heat transfer in the solid mantle was so efficient that the BMO would begin to solidify immediately.

The BMO's lifetime is highly sensitive to the fraction of total internal heating concentrated within it. Assuming the KREEP layer contained all of the radiogenic elements (and thus 50% are in the BMO) increased the lifetime by approximately 150% compared with the nominal case. On the other hand, if the fraction were reduced to 27% (i.e. 3× more concentrated than the bulk mantle), the lifetime reduced by 40% to only 1.6 b.y.

Finally, we considered the effect of a smaller fraction f_{KREEP} that remained near the surface. If all of the KREEP layer fell, the BMO would be 450 km thick, extending to a radius of 800 km for our model's 350-km core. In this case, the BMO lifetime increased by 20% with respect to nominal to 3.1 b.y. Between these two values, the BMO's lifetime is affinely dependent on the magma ocean radius, R_{B}. This is reasonable since heat flow is dependent on area, while the total heat that must be removed is dependent on volume.

Our results, therefore, suggest that a fully molten BMO existed from 4.2 Ga to 1.6 Ga (nominal model), although its possible lifetime spans the range from immediate solidification to continuation at present day given the uncertainty in input parameters. This intermediate age is consistent with a partially molten lower mantle inferred from geophysical measurements (Weber et al., 2011; Harada et al., 2014; Khan et al., 2014).

As anticipated considering the relatively large radius of the BMO and the r^{-3} decay of magnetic dipole field strength with distance above the dynamo region, the resulting surface field strengths are substantially larger than thermochemical core dynamo predictions and significantly more consistent with the observed ancient magnetic field (Fig. 3). The nominal model indicates a maximum surface magnetic field of 4.1 μT, 6.7 μT, and 14.5 μT for the ML, CIA, and MAC scalings, respectively (Fig. 2B). Using the characteristic velocities associated with the three scaling laws and nominal BMO thickness, the minimum electrical conductivity necessary to sustain a dynamo is $3{\cdot}10^3$ S/m, $7{\cdot}10^3$ S/m, and $3{\cdot}10^4$ S/m for the ML, CIA, and MAC scalings, respectively. The critical conductivity values presented are those at 3.56 Ga, the approximate end of the high-field epoch in lunar history. We, therefore, conclude that the BMO can likely sustain a dynamo only if sufficiently metal-rich.

Although solid mantle viscosity played a strong role in determining longevity, it was not found to affect the field strength and minimum conductivity substantially. However, when internal heating was fully concentrated in the KREEP layer, field strengths increased by approximately 20%, while the minimum conductivity reduced by over 20%. f_{KREEP} had the largest effect on the magnetic

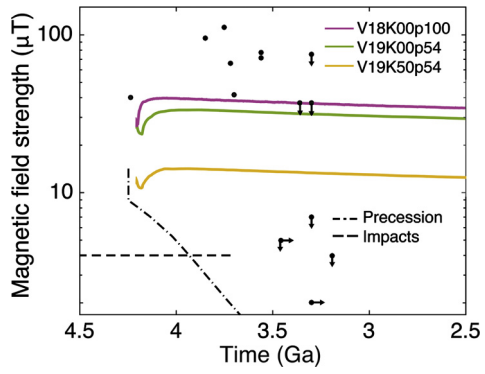

Fig. 3. Estimated surface magnetic field in comparison with observational data (Weiss and Tikoo, 2014). The paleomagnetic field measurements, indicated by the black dots, are accurate to within a factor of approximately five. Downward or rightward arrows indicate that the data point is only an upper bound on field magnitude or sample age, respectively. Three models are presented and utilize the MAC scaling law. The nominal model is shown in yellow. The second model (green) assumes all KREEP material has sunk to the CMB. The final model (magenta) assumes the same, while also using a low solid mantle viscosity and assuming that all radiogenic heating occurs in the KREEP layer. Precession-driven (Dwyer et al., 2011) and impact-driven (Le Bars et al., 2011) core dynamo fields are shown for comparison. In contrast, thermochemical core dynamos produce maximum fields of $\lesssim$1 μT (Stegman et al., 2003; Evans et al., 2014, 2018; Laneuville et al., 2014; Scheinberg et al., 2015).

field since it determines the radius of the BMO. Assuming that all of the KREEP layer sank to the CMB and contains all of the mantle's radiogenic material, the magnetic field scalings span 12–40 μT, with respective critical conductivities of 10^3 S/m to $2{\cdot}10^4$ S/m. The dependence of field strength and minimum conductivity on these parameters is illustrated in Fig. 4.

4. Conclusion

The magnetic field values calculated in this study are consistent, within uncertainty, with the paleomagnetic evidence recorded by the lunar crust in its early history. The field could be further amplified by tidal forces (Dwyer et al., 2011), which would have imparted additional energy to the BMO dynamo, and through interactions with the core (Ziegler and Stegman, 2013).

Past studies have demonstrated that a conventional thermochemical core dynamo would not have been able to produce the inferred paleofields. Exotic mechanisms must therefore be considered. A basal magma ocean dynamo appears uniquely adequate to explain observable evidence, although the hypothesis would require an unusually high conductivity. Further theoretical and experimental work is required to assess whether such conditions could have existed in early lunar history.

The duration of this dynamo has a natural limitation: the high-field epoch ends when *Rm* falls below the critical value as convective vigor and/or ocean thickness decrease. After its demise (which may have occurred long before the BMO solidified), a core dynamo could sustain a lower-strength magnetic field for billions of years after. Thus, an early BMO dynamo in combination with a later thermo-compositional core dynamo driven primarily by inner core solidification provides an elegant and consistent explanation for the complex history of the lunar magnetic field and helps constrain the Moon's evolution.

Acknowledgements

This work was funded with NSF Grant No. 0909206. We thank J. Wisdom for use of computational resources as well as J. Tybur-

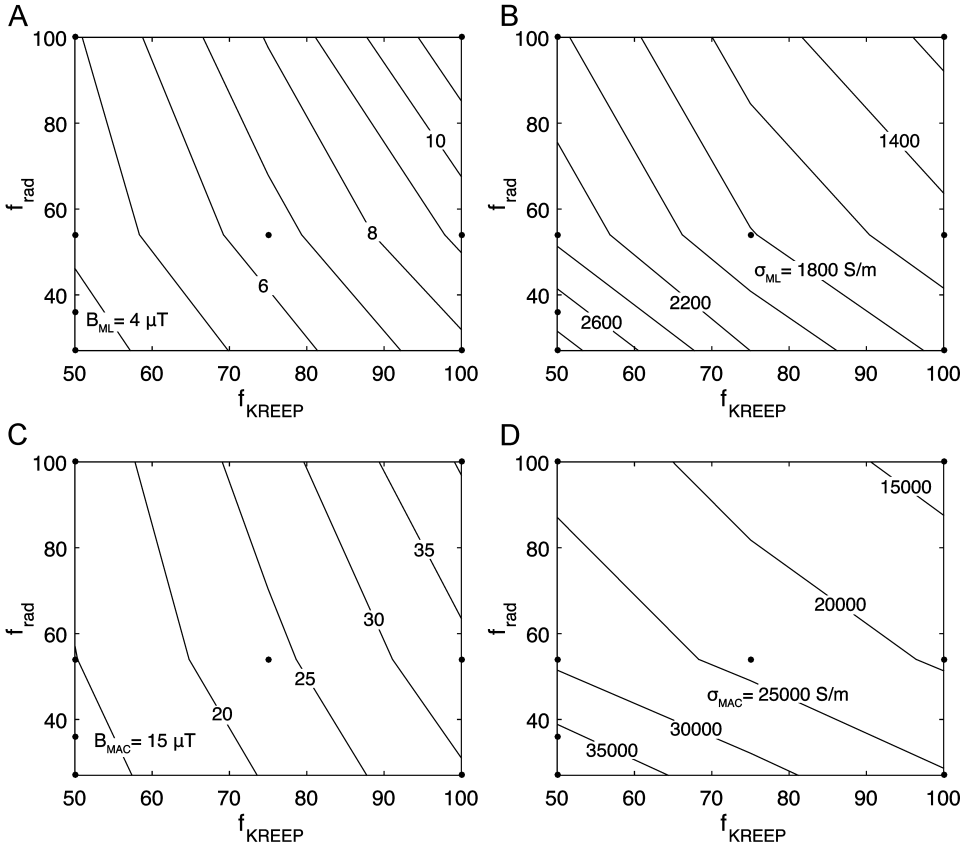

Fig. 4. Contour plots of field strength and critical conductivity as a function of input parameters f_{KREEP} and f_{rad}. **(A)** and **(B)** show, respectively, the predicted magnetic field strength and the minimum conductivity necessary for a dynamo to exist using the ML scaling. Likewise, **(C)** and **(D)** show, respectively, the predicted magnetic field strength and minimum conductivity using the MAC scaling. The dots represent the points in parameter space simulated by our model.

czy, J.-F. Lin, and N. Dygert for fruitful discussions on the electrical conductivity of mantle rocks.

Appendix A. Estimation of fraction of KREEP material to sink

A complete treatment of the problem of lunar overturn is not within the scope of this study. Here we employ a simplified model to demonstrate the plausibility of the KREEP material sinking in full or in part.

In a gravitationally unstable system, a Rayleigh–Taylor instability will develop and result in the dense overlying material sinking. This timescale can be estimated as:

$$\tau_{OT} = \frac{4\pi\mu}{\Delta\rho g d} \tag{A.1}$$

where μ, $\Delta\rho$, g, and d are viscosity, density difference, gravitational acceleration, and layer thickness, respectively (Hess and Parmentier, 1995). However, viscosity is dependent on temperature, and temperature is decreasing as the Moon cools. Hence there is a competition between the timescale of the instability and the timescale of cooling.

Assuming radial symmetry, we use a one-dimensional finite-difference code solving the thermal diffusion equation,

$$\frac{\partial T}{\partial t} = \kappa\nabla^2 T + H(t,r)/\rho c_P \tag{A.2}$$

for temperature T given radiogenic heating $H(t,r)$. The code was benchmarked with the analytic solution of a cooling half-space where $H = 0$.

We consider the time period when the KREEP material has just solidified and is therefore near its melting temperature (assumed as in the text to be 1700 K). By this time, the plagioclase crust would already have developed a conductive temperature profile which we allow to be linear.

Using equation (A.2) to obtain temperature as a function of time and radius (Fig. A1A), we then employ equation (1) to determine the associated local viscosity. We use the viscosity at the top of the layer when evaluating τ_{OT}. Since average viscosity in the layer is lower, this approach will overestimate τ_{OT}.

Roughly speaking, the entire layer will sink if the overturn timescale elapses. Mathematically, complete overturn will occur if there exists a critical time t_c after the onset of the instability such that:

$$\tau_{OT}(t_c) = t_c. \tag{A.3}$$

In other words, t_c is the time required for the layer (or specified fraction of the layer) to overturn, if it will overturn at all. Since τ_{OT} is proportional to μ which is proportional to a reference viscosity μ_0, there will always be some μ_0 for which equation (A.3) is satisfied and some μ_0 for which it is not satisfied. We can there-

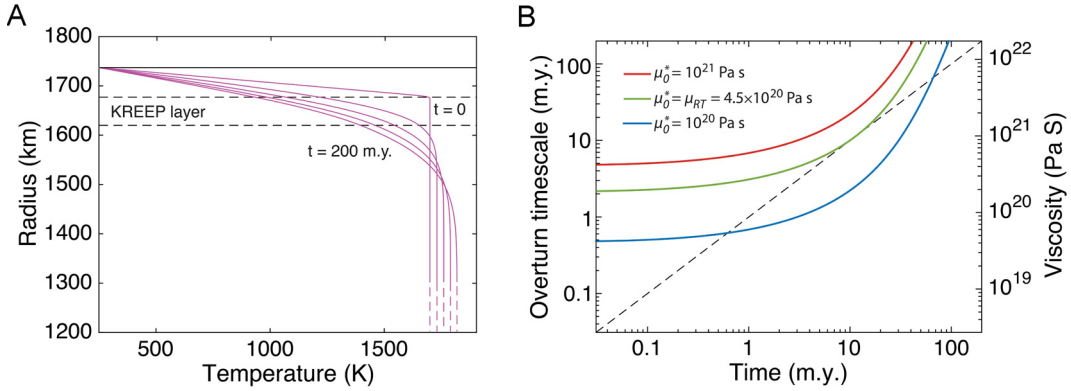

Fig. A1. Simulation of mantle cooling and resulting Rayleigh–Taylor instability timescales. **(A)** Cooling of the one-dimensional conduction thermal diffusion model when 27% of radiogenic material is concentrated in the KREEP layer. The five curves show the thermal profile's evolution from initiation to 50, 100, 150, and 200 m.y. as indicated. **(B)** Viscosity near the top of the KREEP layer and the associated "instantaneous" overturn timescale evolution for the thermal model shown in (A). The three curves are identical except for a differing reference viscosity μ_0^*. Since viscosity μ and overturn timescale τ_{RT} are both directly proportional to μ_0^*, adjusting this value simply translates the curve up or down (on a logarithmic plot). Intersections with the black dashed line, which has a slope of one, indicate complete overturning of the mantle. The blue curve intersects the line at 0.62 m.y.; since complete overturn would have taken 0.62 m.y. or less (τ_{RT} ($t \leq 0.62$ m.y.) ≤ 0.62 m.y.), and 0.62 m.y. elapsed, this implies overturn completion. The red curve, with higher viscosity, never intersects, so complete overturn does not occur. The green curve corresponds to the lowest reference viscosity that will still result in an intersection, μ_{RT}. (For interpretation of the colors in the figure(s), the reader is referred to the web version of this article.)

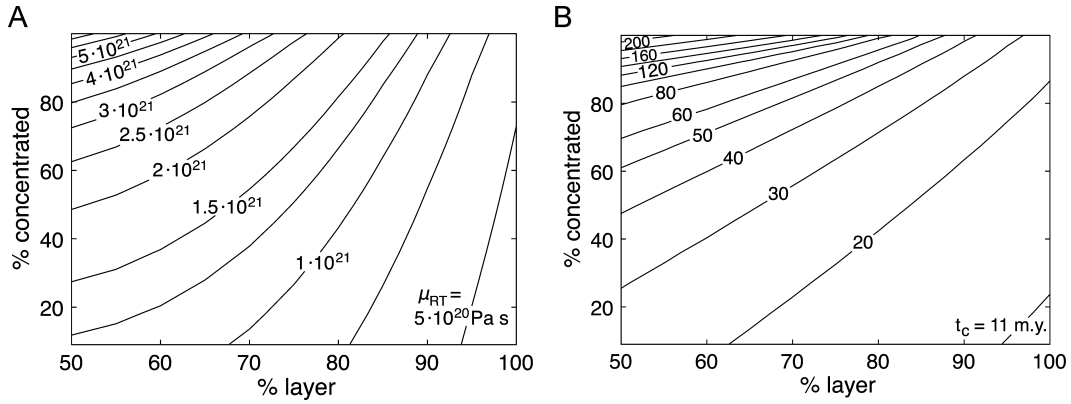

Fig. A2. **(A)** Contour plot of the maximum reference viscosity that would still result in a given fraction of the layer sinking, as a function of concentration of radiogenic elements. **(B)** Contour plot showing the time it would take for overturn to occur assuming that reference viscosity. If 27% of radiogenic elements are concentrated in the layer, then, conservatively speaking, a reference viscosity of $4.1\cdot10^{20}$ Pa s or lower would permit the entire layer to sink.

fore solve for the highest reference viscosity μ_{RT} that would still result in complete overturn (Fig. A1B).

In addition to determining t_c and μ_{RT} for the entire layer, we can also evaluate these values for a subsection of the layer in order to investigate the likelihood of a fraction of the layer sinking. To do that, we assume the fraction of material above the subsection is frozen in place; therefore, in equation (A.1), d is the subsection thickness and μ is the viscosity at the top of the subsection. Since the overlying material is in fact not fixed, this approach will also overestimate τ_{OT}.

We evaluate μ_{RT} and its associated t_c for the overturn of a fraction of the dense layer varied between 50% and 100%. We also vary the fraction of radiogenic elements concentrated in the KREEP layer between 18% (2× bulk mantle concentration) and 100%.

Fig. A2 shows the results. If 27% of radiogenic elements are concentrated in the layer, then, conservatively speaking, a reference viscosity of $4.1{\cdot}10^{20}$ Pa s or lower would permit the entire layer to sink. If 100% of radiogenic elements are concentrated in the layer, then, conservatively speaking, a reference viscosity of $6.3{\cdot}10^{21}$ Pa s or lower would permit 50% of the layer to sink.

Viscosity is poorly constrained, especially considering the possible presence of water and of melt in the newly solidified layer. Crustal thickness, thermal conductivity, and initial temperature will all affect viscosity as well. It is therefore plausible that viscosity was above or below the critical values presented here. Neither near-complete overturn or near-complete retention can be ruled out.

References

Anderson, W.W., Ahrens, T.J., 1994. An equation of state for liquid iron and implications for the earth's core. J. Geophys. Res. 99, 4273–4284.

Bartetzko, A., Delius, H., Pechnig, R., 2005. Effect of compositional and structural variations on log responses of igneous and metamorphic rocks. I: Mafic rocks. Geol. Soc. (Lond.) Spec. Publ. 240 (1), 255–278.

Braginsky, S.I., Roberts, P.H., 1995. Equations governing convection in Earth's core and the geodynamo. Geophys. Astrophys. Fluid Dyn. 79, 1–97.

Buffett, B.A., 2002. Estimates of heat flow in the deep mantle based on the power requirements for the geodynamo. Geophys. Res. Lett. 29, 1566.

Buffett, B.A., Huppert, H.E., Lister, J.R., Woods, A.W., 1996. On the thermal evolution of the Earth's core. J. Geophys. Res. 1996, 7989–8006.

Christensen, U.R., 1984. Convection with pressure- and temperature-dependent non-Newtonian rheology. Geophys. J. R. Astron. Soc. 77, 343–384.

Christensen, U.R., 2010. Dynamo scaling laws and applications to the planets. Space Sci. Rev. 152, 565–590.

Christensen, U.R., Aubert, J., 2006. Scaling properties of convection driven dynamos in rotating spherical shells and application to planetary magnetic fields. Geophys. J. Int. 166, 97–114.

Desai, P.D., 1986. Thermodynamic properties of iron and silicon. J. Phys. Chem. Ref. Data 15, 967–983.

Dwyer, C.A., Stevenson, D.J., Nimmo, F., 2011. An early nutation-driven lunar dynamo. Nature 119, 212–214.

Dygert, N., Lin, J.-F., Marshall, E.W., Kono, Y., Gardner, J.E., 2017. A low viscosity lunar magma ocean forms a stratified anorthic flotation crust with magic poor and rich units. Geophys. Res. Lett. 44, 11282–11291.

Elkins-Tanton, L.T., Burgess, S., Yin, Q.-Z., 2011. The lunar magma ocean: reconciling the solidification process with lunar petrology and geochronology. Earth Planet. Sci. Lett. 304, 326–336.

Evans, A.J., Tikoo, S.M., Andrews-Hanna, J.C., 2018. The case against an early lunar dynamo powered by core convection. Geophys. Res. Lett. 45, 98–107.

Evans, A.J., Zuber, M.T., Weiss, B.P., Tikoo, S.M., 2014. A wet, heterogeneous lunar interior: lower mantle and core dynamo evolution. J. Geophys. Res. 119, 1061–1077.

Garrick-Bethell, I., Weiss, B.P., Shuster, D.L., Tikoo, S.M., Tremblay, M.M., 2017. Further evidence for early lunar magnetism from troctolite 76535. J. Geophys. Res., Planets 122, 76–93.

Hagerty, J.J., Shearer, C.K., Vaniman, D.T., 2006. Heat-producing elements in the lunar mantle: insights from ion microprobe analyses of lunar pyroclastic glasses. Geochim. Cosmochim. Acta 70, 34573476.

Harada, Y., Goossens, S., Matsumoto, K., Yan, J., Ping, J., Noda, H., Haruyama, J., 2014. Strong tidal heating in an ultralow-viscosity zone at the core–mantle boundary of the Moon. Nat. Geosci. 7, 569–572.

Hess, P.C., Parmentier, E.M., 1995. A model for the thermal and chemical evolution of the Moon's interior: implications for the onset of mare volcanism. Earth Planet. Sci. Lett. 134, 501–514.

Karato, S.-I., Wu, P., 1993. Rheology of the upper mantle: a synthesis. Science 260, 771–778.

Khan, A., Connolly, J.A.D., Pommier, A., Noir, J., 2014. Geophysical evidence for melt in the deep lunar interior and implications for lunar evolution. J. Geophys. Res. 119, 2197–2221.

Labrosse, S., 2003. Thermal and magnetic evolution of the Earth's core. Phys. Earth Planet. Inter. 140, 127–143.

Laneuville, M., Wieczorek, M.A., Breuer, D., Aubert, J., Morard, G., Rückriemen, T., 2014. A long-lived lunar dynamo powered by core crystallization. Earth Planet. Sci. Lett. 401, 251–260.

Le Bars, M., Wieczorek, M.A., Karatekin, O., Cebron, D., Laneuville, M., 2011. An impact-driven dynamo for the early Moon. Nature 479, 215–218.

Lin, Y., Tronche, E.J., Steenstra, E.S., van Westrenen, W., 2017a. Evidence for an early wet moon from experimental crystallization of the lunar magma ocean. Nat. Geosci. 10, 14–19.

Lin, Y., Tronche, E.J., Steenstra, E.S., van Westrenen, W., 2017b. Experimental constraints on the solidification of a nominally dry magma ocean. Earth Planet. Sci. Lett. 471, 104–116.

Lister, J.R., 2003. Expressions for the dissipation driven by convection in the Earth's core. Phys. Earth Planet. Inter. 140, 145–158.

Lister, J.R., Buffett, B.A., 1995. The strength and efficiency of thermal and compositional convection in the geodynamo. Phys. Earth Planet. Inter. 91, 17–30.

Meyer, J., Elkins-Tanton, L.T., Wisdom, J., 2010. Coupled thermal-orbital evolution of the early Moon. Icarus 208, 1–10.

Nimmo, F., 2007. Thermal and compositional evolution of the core. In: Olson, P.L. (Ed.), Treatise on Geophysics, vol. 8. Elsevier, pp. 217–241.

Pommier, A., Leinenweber, K., Tasaka, M., 2015. Experimental investigation of the electrical behavior of olivine during partial melting under pressure and application to the lunar mantle. Earth Planet. Sci. Lett. 425, 242–255.

Roberts, P.H., 2007. Theory of the geodynamo. In: Schubert, G. (Ed.), Treatise on Geophysics, vol. 8. Core Dynamics. Elsevier, Amsterdam, pp. 67–105. Ch. 3.

Scheinberg, A., Soderlund, K.M., Schubert, G., 2015. Magnetic field generation in the lunar core: the role of inner core growth. Icarus 254, 62–71.

Shea, E.K., Weiss, B.P., Cassata, W.S., Shuster, D.L., Tikoo, S.M., Gattacceca, J., Grove, T.L., Fuller, M.D., 2012. A long-lived lunar core dynamo. Science 335, 453–456.

Solomatov, V.S., 2007. Magma oceans and primordial mantle differentiation. In: Treatise on Geophysics, vol. 9. Elsevier, pp. 91–120.

Spera, F.J., 1992. Lunar magma transport phenomena. Geochim. Cosmochim. Acta 56, 2253–2265.

Stegman, D.R., Jellinek, A.M., Zatman, S.A., Baumgardner, J.R., Richards, M.A., 2003. An early lunar core dynamo driven by thermochemical mantle convection. Nature 421, 143–146.

Suavet, C., Weiss, B.P., Cassata, W.S., Shuster, D.L., Gattacceca, J., Chan, I., Garrick-Bethell, I., Head, J.W., Grove, T.L., Fuller, M.D., 2013. Persistence and origin of the lunar core dynamo. Proc. Natl. Acad. Sci. 18, 1–6.

Tikoo, S.M., Weiss, B.P., Shuster, D.L., Suavet, C., Wang, H., Grove, T.L., 2017. A two-billion-year history for the lunar dynamo. Sci. Adv. 3, e1700207.

Touloukian, Y.S., Powell, R.W., Ho, C.Y., Klemens, P.G., 1970. Thermophysical Properties of Matter, Volume 1: Thermal Conductivity – Metal Elements and Alloys. Tech. Rep., DTIC Document.

van Kan Parker, M., Sanloup, C., Sator, N., Guillot, B., Tronche, E.J., Perrillat, J.-P., Mezouar, M., Rai, N., Van Westrenen, W., 2012. Neutral buoyancy of titanium-rich melts in the deep lunar interior. Nat. Geosci. 5 (3), 186–189.

Warren, P.H., 1985. The magma ocean concept and lunar evolution. Annu. Rev. Earth Planet. Sci. 13, 201–240.

Weber, R.C., Lin, P.-Y., Garnero, E.J., Williams, Q., Lognonne, P., 2011. Seismic detection of the lunar core. Science 331, 309–312.

Weiss, B.P., Tikoo, S.M., 2014. The lunar dynamo. Science 346, 1246753.

Williams, J.G., Konopliv, A.S., Boggs, D.H., Park, R.S., Yuan, D.N., Lemoine, F.G., Goossens, S., Mazarico, E., Nimmo, F., Weber, R.C., Asmar, S.W., 2014. Lunar interior properties from the GRAIL mission. J. Geophys. Res., Planets 119, 1546–1578.

Zhang, N., Dygert, N., Liang, Y., Parmentier, E.M., 2017. The effect of ilmenite viscosity on the dynamics and evolution of an overturned lunar cumulate mantle. Geophys. Res. Lett. 44, 6543–6552.

Zhang, N., Parmentier, E.M., Liang, Y., 2013. A 3-D numerical study of the thermal evolution of the Moon after cumulate mantle overturn: the importance of rheology and core solidification. J. Geophys. Res., Planets 118, 1789–1804.

Zhong, S., McNamara, A., Tan, E., Moresi, L., Gurnis, M., 2008. A benchmark study on mantle convection in a 3-D spherical shell using CitcomS. Geochem. Geophys. Geosyst. 9, Q10017.

Ziegler, L.B., Stegman, D.R., 2013. Implications of a long-lived basal magma ocean in generating Earth's ancient magnetic field. Geochem. Geophys. Geosyst. 14, 4735–4742.